MEDICAL ROBOTS

Hybrid biomembrane–functionalized nanorobots for concurrent removal of pathogenic bacteria and toxins

Berta Esteban-Fernández de Ávila,* Pavimol Angsantikul,* Doris E. Ramírez-Herrera,*
Fernando Soto, Hazhir Teymourian, Diana Dehaini, Yijie Chen, Liangfang Zhang,† Joseph Wang†

With the rapid advancement of robotic research, it becomes increasingly interesting and important to develop biomimetic micro- or nanorobots that translate biological principles into robotic systems. We report the design, construction, and evaluation of a dual–cell membrane–functionalized nanorobot for multipurpose removal of biological threat agents, particularly concurrent targeting and neutralization of pathogenic bacteria and toxins. Specifically, we demonstrated ultrasound-propelled biomimetic nanorobots consisting of gold nanowires cloaked with a hybrid of red blood cell (RBC) membranes and platelet (PL) membranes. Such hybrid cell membranes have a variety of functional proteins associated with human RBCs and PLs, which give the nanorobots a number of attractive biological capabilities, including adhesion and binding to PL-adhering pathogens (e.g., *Staphylococcus aureus* bacteria) and neutralization of pore-forming toxins (e.g., α-toxin). In addition, the biomimetic nanorobots displayed rapid and efficient prolonged acoustic propulsion in whole blood, with no apparent biofouling, and mimicked the movement of natural motile cells. This propulsion enhanced the binding and detoxification efficiency of the robots against pathogens and toxins. Overall, coupling these diverse biological functions of hybrid cell membranes with the fuel-free propulsion of the nanorobots resulted in a dynamic robotic system for efficient isolation and simultaneous removal of different biological threats, an important step toward the creation of a broad-spectrum detoxification robotic platform.

INTRODUCTION

Tiny robots at the micro- and nanoscale have recently attracted great attention because of their unprecedented features and functions as well as enormous potential applications, especially in the areas of health care and biomedicine (*1*, *2*). These small-scale mobile devices can effectively overcome low Reynolds number viscous drag and Brownian motion by converting locally supplied chemical fuels or external energy (e.g., magnetic, acoustic, or light) into propelling force and movement (*1*, *3*–*5*). More recently, the efficient propulsion of these man-made small robots has been combined with previously unknown functionalities, including advanced motion control, cargo towing and release, chemotactic and collective behavior, and facile surface modification. These features together provide the robots with capabilities for performing diverse tasks in different disciplines, including cell separation, active drug delivery, noninvasive surgery (*2*), environmental remediation (*6*–*10*), and nanoscale fabrication and imaging (*11*). With the rapid advancement of micro- and nanorobots in biomedical research, it becomes important to develop robots with biocompatible and biomimetic surfaces for favorable interfaces and interactions with natural biological subjects. For example, synthetic nanorobots have been integrated recently with motile cells, such as sperm and bacteria (*12*, *13*).

Herein, we report the integration of diverse biological functions from the plasma membranes of two cell types, red blood cells (RBCs) and platelets (PLs), into a single nanorobot surface to create a robust biomimetic nanorobot for multipurpose biodetoxification and concurrent removal of pathogenic bacteria and toxins in particular. In Gram-positive bacterial infections, pathogens normally generate and release a variety of hemolytic toxins, namely, pore-forming toxins (PFTs), into the bloodstream. These toxins actuate pore formation in cell membranes, altering membrane permeability and leading to cellular lysis. This process is one of the major routes of bacterial pathogenesis and results in life-threatening infections in humans (*14*–*16*). From a therapeutic perspective, it would be ideal to remove both the hemolytic toxins and the toxin-produced bacteria to achieve desirable treatment efficacy. However, the major challenge is that the toxins and the bacteria are vastly different physicochemical structures and normally have different biological targets. For instance, PFTs typically target RBCs and destroy them, whereas bacteria may have no specific interactions with RBCs; instead, they bind with other cell types, such as PLs. To solve this problem, we hypothesized that, by coating synthetic nanorobots with a mixture of cell membranes derived from RBCs and PLs, these hybrid biomembrane–functionalized robots will bear lipid membranes and associated functions similar to both RBC and PL membranes. The dual RBC-PL membrane coating will give nanorobots a variety of functional proteins and thus multifaceted biological functions. Therefore, these biomimetic nanorobots are expected to concurrently absorb and remove RBC-targeted PFTs and PL-bound bacteria that produce the PFTs. To test this hypothesis, we adopted a recently developed cell membrane–coating technology to functionalize an acoustic gold nanowire (AuNW)–based nanorobot used as a model of fuel-free robot with potential biomedical applications.

Cell membrane coating has recently emerged as a platform technology that presents a simple top-down approach for functionalizing synthetic subjects with the highly complex functionalities associated with natural cell membranes (*17*–*19*). Specifically, cell membrane–coated nanodevices inherently mimic the surface properties of the source cells and thus bear unique functions, such as disease-relevant targeting ability. For example, RBC membranes can target and absorb toxins, and PL membranes can adhere to pathogens (*14*, *17*–*22*). Initial attempts have integrated nanorobots with singular cell membranes (*23*–*25*). The resulting biomimetic nanorobots combined the advantages of both the dynamic movement of mobile robotics and the functional versatility of the cellular membrane coatings. This coupling greatly

---

Department of NanoEngineering, University of California San Diego, La Jolla, CA 92093, USA.
*These authors contributed equally to this work.
†Correstponding author. Email: josephwang@ucsd.edu (J.W.); zhang@ucsd.edu (L.Z.)

accelerated detoxification processes compared with counterparts based solely on Brownian motion (*12*, *13*, *23*–*25*). For example, RBC membrane–coated robots have demonstrated effective and rapid removal of bacterial toxins and other contaminants (e.g., nerve agents) from biological samples (*23*, *24*). So far, only singular cell membranes have been coupled with nanorobots, providing them with the specific biological function of the corresponding cells while lacking multifaceted functionality. The integration of diverse membrane functionalities from multiple cell types into single mobile nanorobots could result in broader and more robust uses, where the nanorobots could perform multiple complex therapeutic tasks in a single treatment.

In this work, we prepared RBC-PL hybrid membrane–functionalized fuel-free nanorobots (denoted as "RBC-PL-robots"), by enclosing acoustic AuNW robots with the hybrid membranes derived from human RBCs and PLs, for simultaneous targeting and removal of pathogenic bacteria along with toxins secreted by the bacteria (Fig. 1A). The biomimetic robots were fabricated by using a template-assisted AuNW electrochemical deposition protocol (*26*), followed by a dual–cell membrane–cloaking technique (*27*). The dual-membrane coating contained a wide variety of functional proteins associated with human RBCs and PLs, which gave the nanorobot diverse biological functions. Coupling the biological functions of the hybrid membranes with the fuel-free navigation of ultrasound (US)–propelled mobile nanorobots thus resulted in a dynamic biomimetic multifunctional detoxification platform that locally enhanced mass transport and increased directional collisions with biological targets and may represent a unique tool in situations where external mechanical stirring is not possible or desired. The RBC-PL-robots displayed rapid and efficient propulsion in whole blood, with no apparent biofouling, and mimicked the movement of natural motile cells. These mobile nanorobots show both enhanced binding to PL-adhering pathogens and effective neutralization of the pathogen-secreting toxins. Using methicillin-resistant *Staphylococcus aureus* (MRSA) USA300 strain as a model pathogen and α-toxin as well as other PFTs secreted by MRSA bacteria as model toxins, we demonstrated that the RBC-PL-robots offer simultaneous accelerated detoxification of different biocontaminants present in the same sample within minutes. The advanced biomimetic and fuel-free propulsion capabilities of the dual-membrane–functionalized nanorobots may be used for rapid bacteria isolation and efficient neutralization of PFTs in a variety of biomedical and biodefense scenarios. This dual–cell membrane coating represents a unique and robust technique to functionalize nanorobots for potential use in different

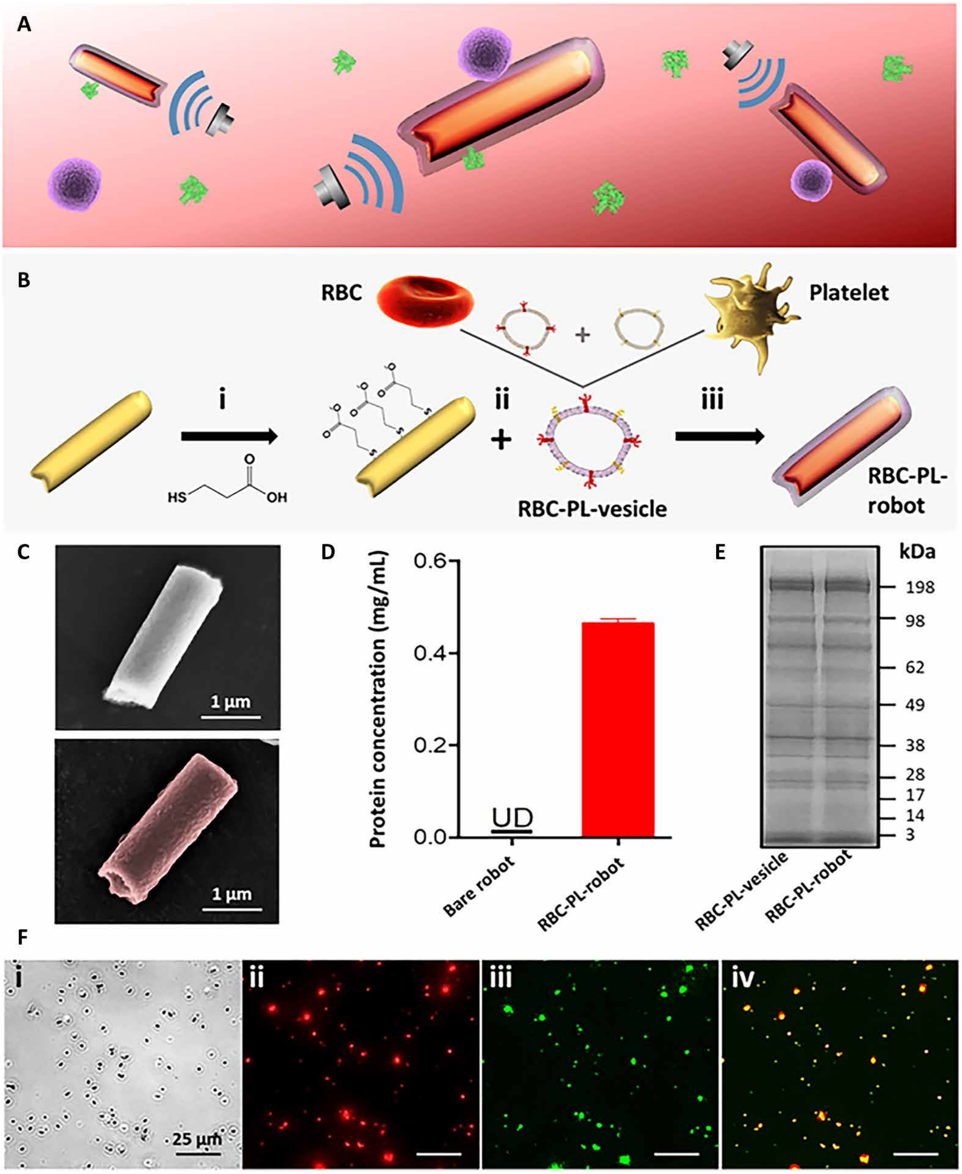

Fig. 1. Preparation and characterization of RBC-PL-robots. (**A**) Schematic of biomimetic robots for binding and removal of threatening biological agents. (**B**) Preparation of RBC-PL-robots: (i) The gold surface of the nanowire (AuNW) robots was modified with MPA; (ii) hybrid membranes were prepared by fusion of RBC membranes and PL membranes (using 1:1 protein weight ratio), and the resulting hybrid membranes were used to coat the MPA-modified nanorobots; (iii) after 5-min sonication, the RBC-PL-robots were obtained. (**C**) SEM images of a bare AuNW robot without hybrid membrane coating (top) and an RBC-PL-robot (bottom). (**D**) The measured weight of protein content on bare robots and RBC-PL-robots (both 20 mg ml^{-1}) stored in 1× PBS at 4°C for 24 hours. UD, undetectable. Error bars represent the SD from three different measurements. (**E**) SDS–polyacrylamide gel electrophoresis analysis of proteins present on the RBC-PL-vesicles and the RBC-PL-robots. The samples were run at equal protein content and stained with Coomassie blue. The RBC-PL-robots used in (D) and (E) were exposed to the acoustic field for 5 min before performing the protein analysis. (**F**) Optical (i) and fluorescent (ii to iv) images of a group of RBC-PL-robots, in which the RBC membranes were labeled with DiD dye (red) and the PL membranes were labeled with FITC (green). Overlay of the DiD and FITC channels is shown in (iv) (yellow).

fields, including targeted drug delivery, immune modulation, and detoxification. Although acoustic propulsion was selected as a model of fuel-free propulsion, the reported dual–cell membrane coating concept can be readily expanded to other types of nanorobots involving different propulsion mechanisms.

RESULTS

Preparation of RBC-PL-robots

The preparation of RBC-PL-robots involved the combination of template-assisted electrodeposition and cell membrane–cloaking techniques. As shown in Fig. 1B, the AuNW robots were prepared by a common membrane-template electrodeposition protocol (see Materials and Methods) (*26*) consisting of gold deposition within the nanopores (400 nm diameter) of a polycarbonate (PC) membrane, followed by the membrane dissolution and release of the resulting AuNWs. The surface of the AuNWs was then modified with 3-mercaptopropionic acid (MPA) (Fig. 1B, i) before membrane coating. In parallel, RBC-PL hybrid membrane–derived vesicles (denoted as "RBC-PL-vesicles"; diameter, 100 to 150 nm) were prepared by fusion of the RBC and PL membranes (1:1 protein weight ratio) during a 5-min ultrasonication (*27*). The resulting RBC-PL-vesicles, having diverse biological capabilities, were mixed with the MPA-modified AuNWs under ultrasonication for 5 min (Fig. 1B, ii). The nanoscale RBC-PL-vesicles, with high surface energy, were prone to bind and fuse onto the AuNW nanorobots to minimize the system's free energy (Fig. 1B, iii). The ultrasonic mixing further enhanced the adsorption of the RBC-PL hybrid membranes onto the AuNWs. The fusion process allowed for the retention of the bilayer structure of the hybrid membranes and the preservation of their protein functions. In addition, because of the large asymmetric negative charge between the ectoplasmic and cytoplasmic surfaces of the hybrid membranes, the outer surface of the membranes was much more negatively charged than the inner surface. Hence, electrostatic repulsion allowed the hybrid membranes to fuse onto the negatively charged robots at the right-side-out orientation (*18*). This orientation of RBC-PL hybrid membranes enabled the selective adsorption and neutralization of PFTs and pathogens and protected the nanorobots from biofouling during movement in complex biological media.

Characterization of RBC-PL-robots

The fabricated RBC-PL-robots were characterized by different techniques. Figure 1C shows the scanning electron microscope (SEM) images of a bare AuNW robot and an RBC-PL-robot (top and bottom, respectively), both with a diameter of 400 nm and a length of 1.5 to 2.0 μm. An SEM image of the bare AuNW is shown in fig. S1. Both SEM images show the asymmetric shape of the robots containing a concave end obtained by the template electrodeposition (*28*). This structural asymmetry allowed each individual nanowire to convert the acoustic steady streaming produced over the surface of the nanowire into axial motion with an independent trajectory, rather than being dragged as an aggregate by the acoustic radiation or flow forces (*26*, *28*, *29*). Other key factors affecting the conversion of the acoustic energy into motion include material density and dimension, because only structures fabricated with relatively dense materials (e.g., Au, Pt, and Ru) and sizes larger than 500 nm have been reported to present autonomous propulsion (*30*, *31*). Although there are multiple fuel-free microrobots (*8*, *32*) and alternative acoustic propulsion mechanisms based on traveling waves (*33*), streaming (*34*), or bubble cavitation (*35*), the present use of acoustically propelled nanowires produced a synergistic effect of enhancing mass transport while preconcentrating the sample in an acoustic levitation plane, thereby enhancing directional collisions between the nanorobot and the biological target. A thin coating can be observed around the RBC-PL-robot corresponding to the membrane coating. We also investigated the RBC-PL-robots in terms of their protein content from the dual–cell membrane coating. For this purpose, the RBC-PL-robots were repeatedly washed with phosphate-buffered saline (PBS) to remove uncoated membranes and exposed to the acoustic field for 5 min, and then a bicinchoninic acid (BCA) protein assay was used to quantify the level of membrane proteins on the nanorobot surface. A protein content of 0.5 mg ml^{-1} was obtained for the RBC-PL-robots, in comparison with the undetectable protein content for the bare nanorobots, using the same robot concentration (20 mg ml^{-1}) (Fig. 1D). Furthermore, gel electrophoresis followed by protein staining showed the protein profile of the purified RBC-PL-vesicles and RBC-PL-robots (Fig. 1E). The protein profile of the coated robots closely matched that of the hybrid membranes, indicating that the RBC-PL membranes can be translocated onto the nanorobot surface without altering their protein profile. To further confirm the presence and cloaking of hybrid membranes onto the surface of AuNW robots, we labeled the RBC and the PL membranes before coating with the dyes 1,1′-dioctadecyl-3,3,3′,3′-tetramethylindodicarbocyanine,4-chlorobenzenesulfonate salt (DiD; excitation/emission = 644/665 nm) and fluorescein isothiocyanate (FITC; excitation/emission = 495/525 nm), respectively. Figure 1F shows optical (i) and fluorescent (ii to iv) images of a group of RBC-PL-robots coated with the DiD-labeled RBC membranes (red) and FITC-labeled PL membranes (green). Full coverage of the nanorobots is illustrated in the fluorescence microscopy images, indicating the successful incorporation of the dye-labeled dual cell membranes onto the robots. The corresponding overlay of the DiD and FITC channels (shown in Fig. 1F, iv) confirmed the effective co-localization of both cell membranes on the same robot, further verifying the successful coating of the AuNW robots with the dual membranes.

Propulsion performance and anti-biofouling property of RBC-PL-robots

The propulsion performance and anti-biofouling ability of the RBC-PL-robots were evaluated by comparing the propulsion speed of the uncoated AuNW robots and the RBC-PL-robots in water and in whole blood, as illustrated from the stack of overlapping microscopy images in Fig. 2 (A and B) (corresponding to movies S1 and S2). The propulsion of bare robots and RBC-PL-robots was examined first in water, as indicated by the 4-s tracking trajectories shown in Fig. 2 (A, i, and B, i, respectively). Both robots displayed efficient propulsion with a high speed in the aqueous medium (51 and 46 μm s^{-1}; Fig. 2C, gray and red bars, respectively). In contrast, when tested in whole blood, the bare robots displayed notable hindered propulsion, with a greatly diminished speed of ~10 μm s^{-1}, nearly independent of the incubation time (right after mixing and after 1-hour incubation in blood) (Fig. 2A, ii and iii). This hindered movement reflects severe protein fouling of the robots. However, the RBC-PL-robots exhibited only a slight speed decrease when incubated in blood, as shown by the 4-s tracking trajectories of Fig. 2B (ii and iii) and demonstrated by the calculated speeds (Fig. 2C; red bars: 38 and 35 μm s^{-1}, respectively). Although the propulsion of the RBC-PL-robots was slightly affected by the blood viscosity, the robot movement in this complex biological environment remained active over the entire 1-hour operation. Overall,

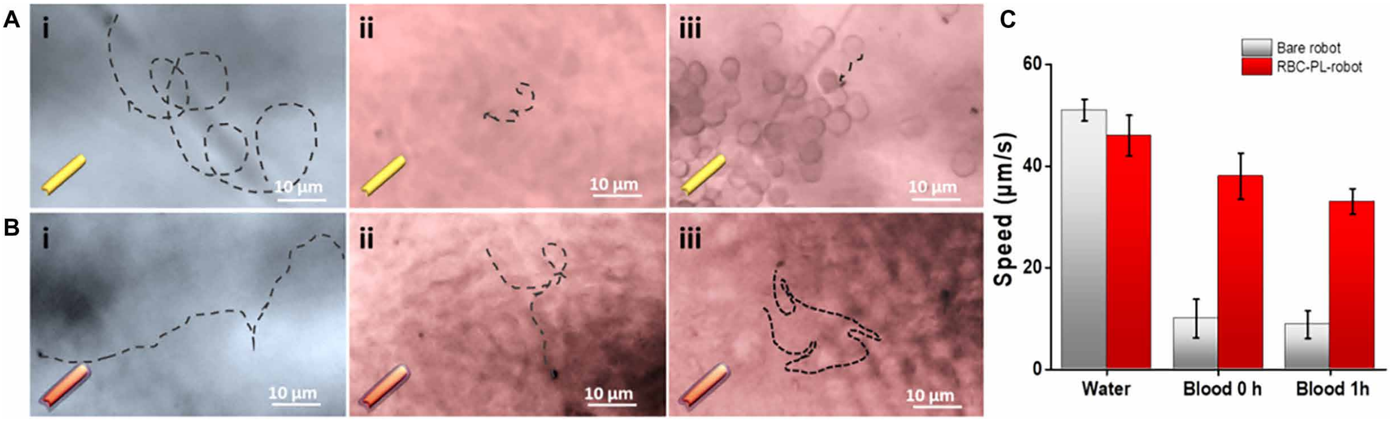

Fig. 2. Propulsion performance and anti-biofouling property of RBC-PL-robots. Tracking trajectories showing the propulsion of bare robots (**A**) and RBC-PL-robots (**B**) in water (i) and after 0- and 1-hour incubation in blood (ii and iii, respectively). (**C**) Comparison of the speed of bare robots with RBC-PL-robots in water and after 0- and 1-hour incubation in blood. The acoustic nanorobots were propelled using a frequency of 2.66 MHz and a voltage of 2.0 V. Error bars estimated as a triple of SD ($n = 3$).

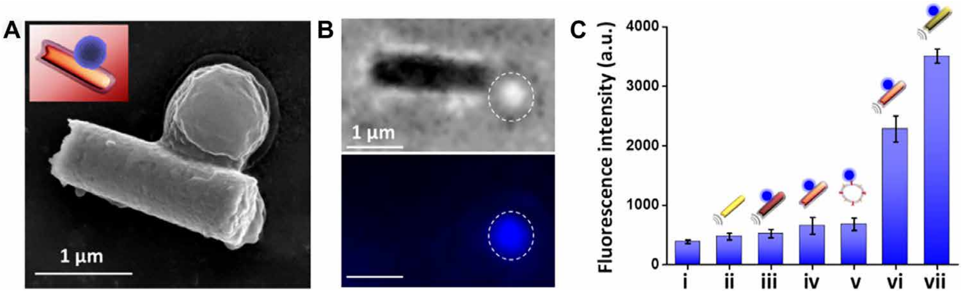

Fig. 3. Binding and isolation of PL-adhering pathogens by RBC-PL-robots. (**A**) SEM image of an MRSA USA300 bacterium attached to an RBC-PL-robot. (**B**) Microscopic images showing the binding of an MRSA USA300 bacterium to an RBC-PL-robot: bright-field image (top) and fluorescence image showing the DAPI-stained bacterium (bottom). (**C**) Normalized fluorescence intensity of DAPI-stained MRSA USA300 bacteria retained on (i) PBS (no robots), (ii) bare robots, (iii) RBC-robots (without PL membranes), (iv) RBC-PL-robots under a static condition (without US), (v) RBC-PL-vesicles, (vi) US-propelled RBC-PL-robots, and (vii) PL-robots (without RBC membranes). PBS, bare robots, RBC-robots, and RBC-PL-vesicles were used as negative controls; PL-robots were used as a positive control. Error bars were estimated as a triple of SD ($n = 3$). Reaction time, 5 min. Biomimetic robots, 10 mg ml^{-1}. MRSA USA300 bacteria, 5×10^8 CFU ml^{-1}.

these data indicate that the natural surface proteins and functions of the RBC-PL hybrid membranes enabled an effective anti-biofouling property of the biomimetic nanorobots, which allows the robots to work in complex physiological fluids continuously.

Binding and isolation of PL-adhering pathogens by RBC-PL-robots

Characterizations of the robot structure and its US propulsion were followed by critical evaluation of the detoxification potential of the biomimetic nanorobots. Initially, the RBC-PL-robots were assessed for selective binding and rapid isolation of PL-adhering pathogens. Such bacteria binding to a PL is a postulated central event in the pathogenesis of infective endocarditis (*36*), and PL-bacterium interactions are also associated with bacterial immune evasion and bacteremia (*37*). In this study, a strain of MRSA expressing a serine-rich adhesin for PL, MRSA USA300 (*36*), was used as a model PL-adhering pathogen. Figure 3A (see also fig. S2) shows an SEM image indicating an MRSA USA300 bacterium binding to an RBC-PL-robot after a 5-min incubation under a US field (2.66 MHz and 2.0 V). To further characterize the robot/MRSA binding and compare it with other different controls, we incubated the RBC-PL-robots (10 mg ml^{-1}) in the MRSA USA300 suspension [5×10^8 colony-forming units (CFU) ml^{-1}] under US for 5 min, followed by collection of the robots through precipitation, fixation of adhered bacteria with formalin, and staining with 4′,6-diamidino-2-phenylindole (DAPI). Subsequently, the amount of bacteria adhered to the RBC-PL-robots was calculated by measuring the DAPI fluorescence intensity. Figure 3B shows microscopic bright-field and fluorescence images (top and bottom, respectively), which further illustrate the specific binding between an MRSA USA300 bacterium and the RBC-PL-robot. The normalized fluorescence intensity of DAPI-stained MRSA USA300 was calculated and compared with other control experiments (Fig. 3C). PBS, bare nanorobots (without cell membrane coating), and RBC-robots (coated with RBC membranes) were used as negative controls and displayed a negligible fluorescent intensity due to the absence of bacterial adhesion (Fig. 3C, i to iii). Low fluorescence intensity values were also observed for MRSA USA300 incubated with RBC-PL-robots under static conditions or with RBC-PL-vesicles (Fig. 3C, iv and v). In contrast, a remarkable fluorescence intensity increment was observed when incubating DAPI-stained MRSA bacteria with US-propelled RBC-PL-robots (vi) or PL-robots (vii, coated only with PL membranes, used as a positive control), reflecting the active bacterial recognition and binding of the PL membranes. DAPI-stained MRSA treated with US-propelled RBC-PL-robots reached a 3.5-fold increase in DAPI fluorescence intensity compared with their static counterparts {Fig. 3C, vi [2283 arbitrary units (a.u.)] versus iv (650 a.u.)}, indicating the importance of US propulsion for rapid bacteria isolation associated with the enhanced directional collisions between the RBC-PL-robots and bacteria under the acoustic field. Overall, these results demonstrate the unique characteristics of the US-propelled biomimetic robots for achieving rapid and selective isolation of PL-adhering pathogens such as MRSA.

Binding and neutralization of PFTs by RBC-PL-robots

After having studied the pathogen binding capacity of the RBC-PL-robots, we evaluated their application as a powered toxin decoy to absorb and neutralize PFTs, a family of toxins that target RBCs by forming pores in cellular membranes, altering their permeability. We first used α-toxin as a model PFT to test the detoxification potential of the RBC-PL-robots. *S. aureus* secretes this toxin as a water-soluble protein, which can spontaneously incorporate into lipid membranes, forming a heptameric structure with a central pore that facilitates uncontrolled permeation of different molecules, finally leading to cell lysis (*38*–*40*). Developing effective strategies for neutralizing α-toxin is of great importance because it has been demonstrated that the inhibition of α-toxin can reduce the severity of *S. aureus* infections (*14*, *41*). To test such detoxification potential, we mixed a fixed amount of commercially purchased purified α-toxin (1.7 μg ml^{-1}) with the RBC-PL-robots and incubated them for 5 min under a US field. Then, the mixed solution was added to a 5% purified RBC solution and incubated for 30 min at 37°C. After this incubation, the 5% RBC solution was centrifuged, and the absorbance of the supernatant was measured at 540 nm to determine the degree of hemolysis. The absorbance value obtained from a 5% RBC solution sonicated for 5 min was considered as 100% hemolysis, which allowed calculating the relative hemolysis percentage of all the samples (Fig. 4). The supernatant of RBCs incubated with free α-toxin at the same concentration was used as a positive control (Fig. 4A, i), which gave a relative hemolysis close to 100% (Fig. 4B, i). However, substantial lower hemolysis (5.5%) was observed when using US-propelled RBC-PL-robots in the toxin solution (Fig. 4, A and B, iii). These results confirmed the effective binding of the membrane-coated robots to the toxin and indicated that the efficient US propulsion in the α-toxin solution facilitated the number of robot-toxin contacts, improving the toxin absorption and its neutralization. This hemolysis percentage was slightly larger than the one obtained from samples treated with US-propelled RBC-robots (Fig. 4, A and B, iv). PBS without toxin was included as a negative control (Fig. 4, A and B, v). A 4.5 times lower hemolysis was found when using US-propelled RBC-PL-robots compared with the use of the RBC-PL-robots under static conditions (Fig. 4, A and B, ii versus iii), highlighting the important effect of the robot propulsion upon the efficiency of the detoxification process.

To further examine the binding of PFTs to RBC-PL-robots and the following neutralization, we performed similar experiments using toxins naturally secreted from MRSA USA300 (Fig. 4, C and D), including α-toxin, Panton-Valentine leukocidin, and γ-toxin (*42*). In this experiment, MRSA USA300 bacteria were grown for 8 hours, and at this time, an aliquot of the bacterial suspension was treated for 5 min with the US-propelled RBC-PL-robots or the other controls (i to v). After each treatment, the bacterial suspension was centrifuged, and 50 μl of the supernatant containing PFTs was mixed with 5% purified RBC solution to quantify its hemolytic activity. Similar to the previous results, the US-propelled RBC-PL-robots produced lower hemolysis when compared with static RBC-PL-robots (17% versus 40%; Fig. 4, C and D, iii versus iv), demonstrating the effective action of the propulsion. Under the acoustic field, the collective propulsion of the RBC-PL-robots can dramatically accelerate their binding with PFT mixture, thus enhancing the neutralization process. A tendency in the hemolysis percentage similar to the one obtained with commercial toxin was found for the rest of the controls (Fig. 4, C and D, i, iii, and iv). The absorbance spectra of oxyhemoglobin after incubation with purified commercial α-toxin or a cocktail of bacteria-secreted PFTs in the different control experiments are shown in figs. S3 and S4, respectively. Overall, the results of Fig. 4 demonstrate that cloaking RBC-PL membranes onto the AuNW robots and moving these biomimetic robots under a US field result in dynamic detoxification vehicles that can efficiently remove PFTs from their environment.

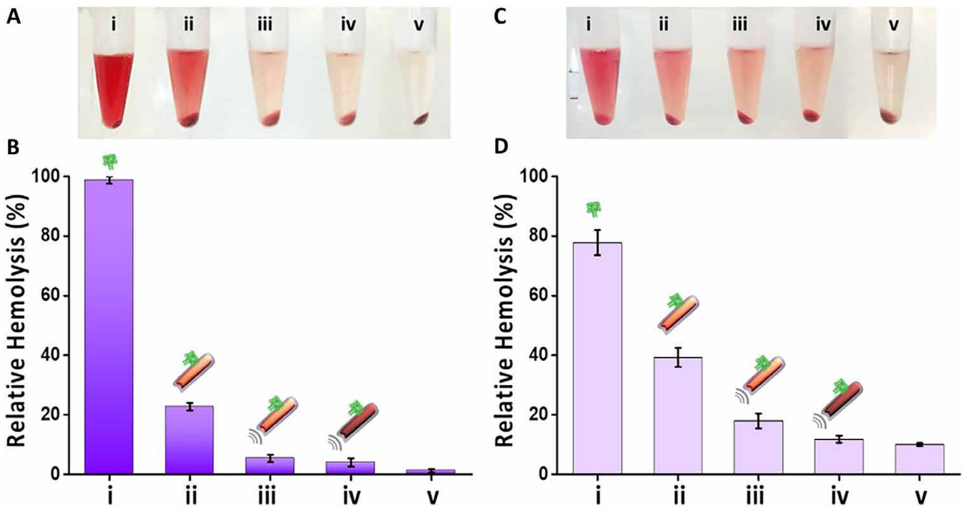

Fig. 4. Binding and neutralization of α-toxin and other PFTs by RBC-PL-robots. (**A**) Images of centrifuged 5% RBC solution after incubation with α-toxin in (i) PBS, (ii) static RBC-PL-robots, (iii) US-propelled RBC-PL-robots, and (iv) US-propelled RBC-robots. PBS without α-toxin (v) was used as a control. (**B**) Hemolysis quantification of the samples shown in (A). (**C**) Images of centrifuged 5% RBC solution after incubation with PFTs (50 μl) produced by MRSA bacteria (after 8-hour incubation) in (i) PBS, (ii) static RBC-PL-robots, (iii) US-propelled RBC-PL-robots, and (iv) US-propelled RBC-robots. PBS without PFTs (v) was used as a control. (**D**) Hemolysis quantification of the samples shown in (C). Error bars estimated as a triple of SD (*n* = 3). Treatment time with samples, 5 min; hemolysis incubation time (5% RBC solution plus PFTs), 30 min at 37°C.

Concurrent removal of bacteria and bacteria-secreting PFTs by RBC-PL-robots

To further examine the dual detoxification ability of these biomimetic nanorobots for binding and isolation of PL-adhering pathogens and neutralization of bacterial toxins, we performed a combined application for MRSA targeting and PFT neutralization (Fig. 5A). In this specific study, the RBC-PL-robots were incorporated with a nickel segment to enable the magnetic separation of the robots after the treatment (fig. S5). To test the combined detoxification action, we compared an MRSA bacterial sample treated with US-propelled RBC-PL-robots with a nontreated bacterial control (Fig. 5, red versus blue). A detailed schematic showing the experimental protocol followed to perform the combined application is shown in fig. S6 (see also Materials and Methods). Briefly, we took two aliquots of MRSA USA300 bacteria from the same culture: One was treated by US-propelled RBC-PL-robots, and one served as an untreated control.

Before performing the robot treatment, the optical density at a wavelength of 600 nm (OD_{600}) and hemolysis percentage were calculated for aliquots taken from both MRSA samples. As shown in Fig. 5 (B and C), both OD_{600} and hemolysis values were very similar for both bacteria samples before the treatment. Afterward, RBC-PL-robots were added to the bacterial suspension under a US field for 5 min. After the robot treatment, the robots were magnetically separated from the bacterial suspension. Then, the treated bacterial sample and the nontreated control sample were grown for 10 hours under the same conditions. The OD_{600} of both samples was monitored every hour during the first 6 hours and then every 2 hours until the end of the experiment to construct the respective curves (Fig. 5D). In parallel, aliquots of both bacterial samples were collected and centrifuged, saving the supernatants to perform the hemolysis assay (Fig. 5, C and E). As shown in Fig. 5 (B and C, red columns), both the OD and hemolysis values notably decreased in the RBC-PL-robot sample at the 0-hour time point (right after the 5-min robot treatment or nontreatment control, indicated by black arrows). Specifically, in the robot-treated sample, the OD and the hemolysis decreased 3.1 and 2.2 times, respectively, when compared with the control sample (Fig. 5, B and C, red versus blue columns). These results demonstrate the rapid and effective detoxification ability of the RBC-PL-robots, which can simultaneously bind to MRSA bacteria and neutralize the secreted PFTs from the same sample in a single treatment step.

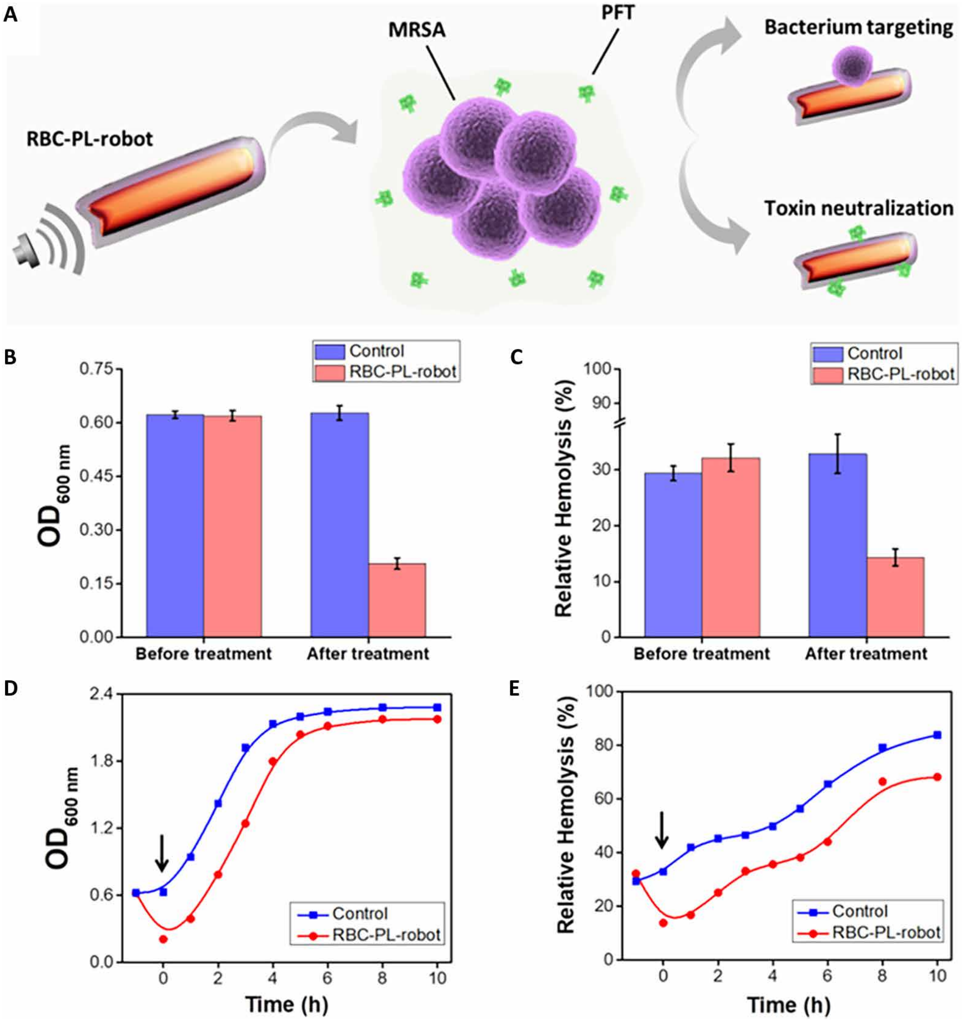

Fig. 5. In situ concurrent removal of MRSA bacteria and MRSA-secreting PFTs by RBC-PL-robots. (**A**) Schematic of RBC-PL-robots for bacteria targeting and PFT neutralization. (**B**) Optical density values (OD_{600}) of MRSA bacteria obtained before and after treatment (blue, without robots; red, RBC-PL-robots). (**C**) Relative hemolysis percentages of PFTs obtained before and after treatment (blue, without robots; red, RBC-PL-robots). Error bars estimated as a triple of SD (n = 3). (**D**) MRSA bacterial growth curves (indicated by OD_{600}) versus incubation time for nontreated bacteria and bacteria treated with RBC-PL-robots. (**E**) Corresponding relative hemolysis curves versus incubation time for nontreated bacteria and bacteria treated with RBC-PL-robots. Arrows indicate first measurement right after treatment.

DISCUSSION

In summary, we have demonstrated that the use of dual cell membranes to modify synthetic nanorobots represents a versatile approach for interfacing natural and synthetic biomaterials to form biomimetic robots. The synergy of combining hybrid biological membranes with mobile robots leads to a powerful platform for diverse biomedical applications. In particular, the biomimetic RBC-PL-robots reported in this proof-of-concept work consisted of an acoustic AuNW robot (selected as a model of fuel-free robots) cloaked with RBC-PL hybrid membranes. The resulting biomimetic fuel-free robots offer a one-step detoxification treatment for simultaneous bacterium targeting and toxin neutralization. Such hybrid cell membrane–coated nanorobots can thus act as a robust mobile therapeutic device capable of accelerating multiple processes, including bacterial detoxification and toxin neutralization. In this work, such capability to accelerate multiple processes was demonstrated for the binding and removal of PL-adhering pathogens (e.g., *S. aureus* bacteria) and neutralization of bacterium-secreting PFTs (e.g., α-toxin). The functional proteins expressed on the hybrid cell membranes allow the robots to be used for detoxification of virulent pathogens and bacterial toxins from biological environments, as illustrated by the rapid targeting and isolation of MRSA USA300 bacteria and neutralization of α-toxin and other PFTs. Our results also demonstrate that the RBC-PL-robots enabled concurrent detoxification of different biocontaminants present in the same sample within minutes. Coupling the biological functionalities of the RBC-PL hybrid membranes with the rapid fuel-free propulsion of the nanorobots thus led to an efficient detoxification system. Moreover, the anti-biofouling property of the membrane coating allows efficient, rapid, and prolonged fuel-free propulsion of the biomimetic robots in complex biological media, including whole blood. Although the dual-membrane coating concept has been demonstrated in connection with US-powered nanowire robots, the technology could be readily adapted to a wide range of nanorobots with different propulsion mechanisms. Coating nanorobots with multifunctional biomembranes imparts important capabilities to robotic technology that are difficult to achieve with uncoated robots.

Although this proof-of-concept work is still at an early stage and requires further improvement and evaluations of the cell membrane–coated robots before their potential uses, it opens the door to the use of fuel-free biomimetic nanorobots as an active broad-spectrum biodetoxification platform. Overall, the ability to concurrently remove pathogenic bacteria and toxins of these biomimetic nanorobots offers considerable interest for diverse therapeutic and detoxification applications. Such biomimetic nanorobots that integrate natural cellular functions with synthetic nanomachines are expected to provide opportunities and inspire ideas for rapidly emerging robotic research and development.

MATERIALS AND METHODS

Nanorobot fabrication

The AuNW robots were prepared by a common membrane-template electrodeposition protocol. A thin gold film was first sputtered on one side of the porous PC membrane template containing 400-nm-diameter nanopores (catalog no. 110407, Whatman Nuclepore) to serve as a working electrode. The membrane was assembled in a Teflon plating cell with aluminum foil serving as an electrical contact for the subsequent electrodeposition. A sacrificial silver layer was electrodeposited into the branched area of the PC membrane using a charge of 0.1 C and a potential of −0.90 V (versus a Ag/AgCl reference electrode, along with a Pt wire as a counter electrode). Subsequently, Au was plated by using a commercial gold plating solution (Orotemp 24 RTU Rack; Technic Inc., Anaheim, CA) at −1.0 V (versus Ag/AgCl), with a charge of 1.5 C. The sputtered gold was removed by mechanical polishing using 3- to 4-μm alumina powder. The silver sacrificial layer was removed by chemical etching using a cotton tip applicator soaked with 8 M HNO_3 solution. The removal of this sacrificial layer helped to create the concave shape in one end of the gold wire nanorobot. The resulting AuNWs had a length between 1.5 and 2 μm. The PC membrane was then dissolved in a pure methylene chloride solution for 30 min; this process was performed two times to completely release the AuNWs. The resulting nanorobots were separated from the solution by centrifugation at 8000 rpm for 5 min and washed two times with isopropanol, two times with ethanol, and three times with ultrapure water (18.2 megohm cm). Between washing steps, the nanorobot solution was centrifuged at 8000 rpm for 3 min. All AuNWs were stored in 1 ml of ultrapure water at room temperature until use. Magnetic robots were prepared following a similar protocol. A sacrificial silver layer was electrodeposited using a charge of 0.1 C and a potential of −0.90 V (versus a Ag/AgCl reference electrode, along with a Pt wire as a counter electrode). Subsequently, Au was plated at −1.0 V (versus Ag/AgCl) using a charge of 0.6 C, followed by Ni electrodeposition at −1.3 V (versus Ag/AgCl) using a charge of 0.4 C. Then, Au was electrodeposited again (−1.0 V and 0.6 C), and the rest of the protocol was performed as described above.

RBC-PL-robot preparation

RBC-PL-robots were prepared by enclosing AuNW robots with the dual plasma membranes derived from RBCs and PLs. Human RBC membranes were derived from whole blood (BioreclamationIVT) as previously described (*43*). Briefly, whole blood was centrifuged at 800*g* for 5 min at 4°C, and the serum and buffy coat were discarded. The remaining RBC pellet was then treated with hypotonic medium to remove hemoglobin. After three hypotonic treatment and wash cycles, the pink pellet of RBC membranes was obtained and stored at −80°C until use. Human PL membranes were prepared from PL-rich plasma (San Diego Blood Bank) following previously described methods (*22*). After obtaining purified PLs, PL membranes were derived using a repeated freeze-thaw process and washed by centrifugation in PBS solution mixed with protease inhibitor tablets. Aliquots of suspensions were first frozen at −80°C, thawed at room temperature, and pelleted by centrifugation at 4000*g* for 3 min. After three repeated washes, the pelleted PL membranes were suspended in water and stored at −80°C until use. After having isolated both RBC and PL membranes, the hybrid membranes were prepared via fusion of both membranes (1:1 protein weight ratio) under 5-min ultrasonication (42 kHz, 100 W).

In parallel, the surface of the AuNWs was modified with 0.25 mM MPA (Sigma-Aldrich) through overnight incubation to introduce negative charges onto the gold surface. After the incubation, the AuNWs were washed with deionized water three times, repeating centrifugation processes (8000 rpm, 3 min) between each washing step. Then, the MPA-AuNWs were coated with the resulting hybrid membranes after 5-min ultrasonication (42 kHz, 100 W).

RBC-PL-robot characterization

SEM images of bare and RBC-PL-robots were obtained with a Philips XL30 environmental scanning electron microscope instrument using an acceleration voltage of 10 kV. To further confirm the presence and cloaking of RBC-PL hybrid membranes onto the surface of the AuNW robots, we labeled RBC membranes with DiD (excitation/emission = 644/665 nm; Sigma-Aldrich), and PL membranes were labeled with FITC (excitation/emission = 495/525 nm; Sigma-Aldrich) before being coated on the AuNWs. Fluorescence microscopy images were captured by using an EVOS FL microscope coupled with 20× and 40× microscope objectives.

To determine the protein content of the RBC-PL-robots, we centrifuged both bare robots and RBC-PL-robots (20 mg ml^{-1}) and resuspended them with 1× PBS three times. After that, the RBC-PL-robots were exposed to the acoustic field for 5 min, and then a BCA colorimetric assay (Sigma-Aldrich) was used to quantitatively measure the level of membrane proteins on the nanorobot surface. Briefly, the purple-colored reaction product of this assay is formed by the chelation of two molecules of BCA with one cuprous ion, and this water-soluble complex exhibits a strong absorbance at 562 nm that is nearly linear with increasing protein concentrations. Gel electrophoresis followed by protein staining with Coomassie blue was also performed. The RBC-PL hybrid membrane and RBC-PL-robot samples containing equivalent total proteins were prepared in lithium dodecyl sulfate sample loading buffer (Invitrogen). The samples were then separated on a 4 to 12% bis-tris 17-well MiniGel in Mops running buffer using a Novex XCell SureLock Electrophoresis System (Life Technologies). Last, the protein columns were stained according to the manufacturer's protocol.

Ultrasound equipment and propulsion studies

The acoustic cell setup consisted of a piezoelectric transducer (Ferroperm PZ26 disk; 10 mm diameter, 0.5 mm thickness) responsible for the generation of US waves, attached by conductive epoxy glue to the bottom center of a steel plate (50 mm by 50 mm by 0.94 mm); the steel plate was covered with a 240-μm Kapton tape protective layer that contains a circular reservoir at the center (5 mm). A glass slide was used to cover the reservoir for US reflection and to protect the sample. The continuous US sine wave was applied via a piezoelectric transducer, through an Agilent 15-MHz arbitrary waveform generator, in connection to a homemade power amplifier. All experiments were performed by mixing the RBC-PL-robots with corresponding media (water, PBS, or whole blood) or samples (MRSA USA300 or toxins) and by applying a continuous sine wave form that had a frequency of 2.66 MHz and a voltage amplitude of 2.0 V. Videos were captured using a CoolSNAP HQ2 camera, with 20× and 40× objectives (unless mentioned otherwise), and acquired at 10 frames per second using the MetaMorph 7.1 software (Molecular Devices, Sunnyvale, CA). The particle displacement image stacking was performed using ImageJ software and Flow Trace Plugin (*44*).

Binding and isolation of PL-adhering pathogens

RBC-PL-robots were assessed for selective binding and rapid isolation of PL-adhering pathogens using MRSA USA300 (BAA-1717; American Type Culture Collection) as a model pathogen. The bacteria were cultured on tryptic soy broth (TSB) agar (Becton, Dickinson and Company) overnight at 37°C. A single colony was inoculated in TSB medium at 37°C in a rotary shaker. Overnight culture was refreshed in TSB medium at a 1:100 dilution at 37°C under shaking for another 3 hours. RBC-PL-robots (10 mg ml^{-1}) were mixed with the bacterial suspension (5×10^8 CFU ml^{-1}), and they were incubated for 5 min under a US field (2.66 MHz and 2.0 V). After the US incubation, the robots were recollected through precipitation, and the adhered bacteria were fixed with formalin and stained with DAPI (Sigma-Aldrich).

Binding and neutralization of PFTs

RBC-PL-robots were tested as a toxin decoy to absorb and neutralize PFTs using α-toxin as a model toxin. A fixed amount of commercial α-toxin (1.7 μg ml^{-1}; IBT Bioservices) was mixed with the RBC-PL-robots (10 mg ml^{-1}) and incubated under a US field for 5 min (2.66 MHz and 2.0 V). After the US treatment, the mixed solution was added to a 5% purified RBC solution and incubated for 30 min at 37°C. After such incubation, the 5% RBC solution was centrifuged, and the absorbance of the supernatant was measured at 540 nm to determine the degree of hemolysis (corresponding to the absorbance spectra of oxyhemoglobin).

To perform the experiments using toxins naturally secreted from MRSA USA300 bacteria, we refreshed overnight bacterial culture in TSB medium at a 1:100 dilution at 37°C under shaking for another 8 hours. The bacterial suspension was centrifuged at 5000*g* for 5 min to collect the culture supernatant. We treated 50 μl of bacterial culture medium containing secreted PFTs with the US-propelled RBC-PL-robots (10 mg ml^{-1}; 2.66 MHz and 2.0 V) and the rest of the controls for 5 min. After treatment and centrifugation, the supernatant from each group was collected and measured for the degree of hemolysis.

Concurrent removal of bacteria and bacteria-secreting PFTs

To test the combined detoxification action of the RBC-PL-robots, we took two aliquots of MRSA USA300 bacteria from the same liquid culture to perform the RBC-PL-robot treatment and to serve as a nontreated control, respectively. Before performing the robot treatment, OD_{600} and hemolysis percentage were measured for aliquots taken from both MRSA samples. Afterward, magnetic RBC-PL-robots (10 mg ml^{-1}) were added to the bacterial suspension (5×10^8 CFU ml^{-1}) under a US field for 5 min (2.66 MHz and 2.0 V). After the robot treatment, the RBC-PL-robots were magnetically separated from the bacterial suspension. Then, the treated bacterial sample and the nontreated control sample were grown for 10 hours under the same conditions. The OD_{600} of both bacterial samples was monitored every hour during the first 6 hours and then every 2 hours until the end of the experiment. In parallel, 50-μl aliquots of both bacterial samples were collected and centrifuged (13,200 rpm, 5 min), saving the supernatants to perform the hemolysis assay (5% RBC solution plus α-toxin, 30 min at 37°C). The relative hemolysis percentages were calculated considering 100% hemolysis, the absorbance value obtained from 5% RBC solution sonicated for 5 min. All the hemolysis studies were performed in the presence of 200 nM 1,4-dithiothreitol (Sigma-Aldrich).

SUPPLEMENTARY MATERIALS

robotics.sciencemag.org/cgi/content/full/3/18/eaat0485/DC1

Fig. S1. SEM images of bare AuNW robots along with the corresponding EDX analysis showing the Au nanorobots' body.

Fig. S2. SEM images of MRSA USA300 bacteria attached to RBC-PL-robots.

Fig. S3. Absorbance spectra of oxyhemoglobin after incubation with commercial purified α-toxin under different conditions.

Fig. S4. Absorbance spectra of oxyhemoglobin after incubation with a cocktail of PFTs produced by MRSA bacteria under different conditions.

Fig. S5. Characterization of bare Au/Ni/Au NW robots.

Fig. S6. Experimental protocol followed to perform the combined application of the RBC-PL-robots: MRSA targeting and PFT neutralization.

Movie S1. Propulsion performance of bare robots in water and whole blood under a US field.

Movie S2. Propulsion performance of RBC-PL-robots in water and whole blood under a US field.

REFERENCES AND NOTES

1. J. Wang, *Nanomachines: Fundamentals and Applications* (Wiley-VCH, 2013).
2. J. Li, B. Esteban-Fernández de Ávila, W. Gao, L. Zhang, J. Wang, Micro/nanorobots for biomedicine: Delivery, surgery, sensing, and detoxification. *Sci. Robot.* **2**, eaam6431 (2017).
3. W. F. Paxton, K. C. Kistler, C. C. Olmeda, A. Sen, S. K. St. Angelo, Y. Cao, T. E. Mallouk, P. E. Lammert, V. H. Crespi, Catalytic nanomotors: Autonomous movement of striped nanorods. *J. Am. Chem. Soc.* **126**, 13424–13431 (2004).
4. X. Yan, Q. Zhou, M. Vincent, Y. Deng, J. Yu, J. Xu, T. Xu, T. Tang, L. Bian, Y.-X. J. Wang, K. Kostarelos, L. Zhang, Multifunctional biohybrid magnetite microrobots for imaging-guided therapy. *Sci. Robot.* **2**, eaaq1155 (2017).
5. W. Wang, L. A. Castro, M. Hoyos, T. E. Mallouk, Autonomous motion of metallic microrods propelled by ultrasound. *ACS Nano* **6**, 6122–6132 (2012).
6. W. Gao, J. Wang, The environmental impact of micro/nanomachines: A review. *ACS Nano* **8**, 3170–3180 (2014).
7. D. Vilela, M. M. Stanton, J. Parmar, S. Sánchez, Microbots decorated with silver nanoparticles kill bacteria in aqueous media. *ACS Appl. Mater. Interfaces* **9**, 22093–22100 (2017).
8. M. Hoop, Y. Shen, X-Z. Chen, F. Mushtaq, L. M. Iuliano, M. S. Sakar, A. Petruska, M. J. Loessner, B. J. Nelson, S. Pané, Magnetically driven silver-coated nanocoils for efficient bacterial contact killing. *Adv. Funct. Mater.* **26**, 1063–1069 (2016).
9. J. Simmchen, A. Baeza, A. Miguel-Lopez, M. M. Stanton, M. Vallet-Regi, D. Ruiz-Molina, S. Sánchez, Dynamics of novel photoactive AgCl microstars and their environmental applications. *ChemNanoMat* **3**, 65–71 (2017).
10. J. Parmar, K. Villa, D. Vilela, S. Sánchez, Platinum-free cobalt ferrite based micromotors for antibiotic removal. *Appl. Mater. Today* **9**, 605–611 (2017).
11. J. Li, W. Liu, T. Li, I. Rozen, J. Zhao, B. Bahari, B. Kante, J. Wang, Swimming microrobot optical nanoscopy. *Nano Lett.* **16**, 6604–6609 (2016).
12. C. Chen, X. Chang, P. Angsantikul, J. Li, B. Esteban-Fernández de Ávila, E. Karshalev, W. Liu, F. Mou, S. He, R. Castillo, Y. Liang, J. Guan, L. Zhang, J. Wang, Chemotactic guidance of synthetic organic/inorganic payloads functionalized sperm micromotors. *Adv. Biosyst.* **2**, 1700160 (2018).
13. O. Felfoul, M. Mohammadi, S. Taherkhani, D. de Lanauze, Y. Z. Xu, D. Loghin, S. Essa, S. Jancik, D. Houle, M. Lafleur, L. Gaboury, M. Tabrizian, N. Kaou, M. Atkin, T. Vuong, G. Batist, N. Beauchemin, D. Radzioch, S. Martel, Magneto-aerotactic bacteria deliver drug-containing nanoliposomes to tumour hypoxic regions. *Nat. Nanotechnol.* **11**, 941–947 (2016).
14. C.-M. J. Hu, R. H. Fang, J. Copp, B. T. Luk, L. Zhang, A biomimetic nanosponge that absorbs pore-forming toxins. *Nat. Nanotechnol.* **8**, 336–340 (2013).

15. C. J. Rosado, S. Kondos, T. E. Bull, M. J. Kuiper, R. H. P. Law, A. M. Buckle, I. Voskoboinik, P. I. Bird, J. A. Trapani, J. C. Whisstock, M. A. Dunstone, The MACPF/CDC family of pore-forming toxins. *Cell. Microbiol.* **10**, 1765–1774 (2008).
16. B. F. C. Kafsack, J. D. O. Pena, I. Coppens, S. Ravindran, J. C. Boothroyd, V. B. Carruthers, Rapid membrane disruption by a perforin-like protein facilitates parasite exit from host cells. *Science* **323**, 530–533 (2009).
17. J.-G. Piao, L. Wang, F. Gao, Y.-Z. You, Y. Xiong, L. Yang, Erythrocyte membrane is an alternative coating to polyethylene glycol for prolonging the circulation lifetime of gold nanocages for photothermal therapy. *ACS Nano* **8**, 10414–10425 (2014).
18. W. Gao, C.-M. J. Hu, R. H. Fang, B. T. Luk, J. Su, L. Zhang, Surface functionalization of gold nanoparticles with red blood cell membranes. *Adv. Mater.* **25**, 3549–3553 (2013).
19. S. Aryal, C.-M. J. Hu, R. H. Fang, D. Dehaini, C. Carpenter, D.-E. Zhang, L. Zhang, Erythrocyte membrane-cloaked polymeric nanoparticles for controlled drug loading and release. *Nanomedicine* **8**, 1271–1280 (2013).
20. Z. Pang, C.-M. J. Hu, R. H. Fang, B. T. Luk, W. Gao, F. Wang, E. Chuluun, P. Angsantikul, S. Thamphiwatana, W. Lu, X. Jiang, L. Zhang, Detoxification of organophosphate poisoning using nanoparticle bioscavengers. *ACS Nano* **9**, 6450–6458 (2015).
21. F. Wang, W. Gao, S. Thamphiwatana, B. T. Luk, P. Angsantikul, Q. Zhang, C.-M. J. Hu, R. H. Fang, J. A. Copp, D. Pornpattananangkul, W. Lu, L. Zhang, Hydrogel retaining toxin-absorbing nanosponges for local treatment of methicillin-resistant *Staphylococcus aureus* infection. *Adv. Mater.* **27**, 3437–3443 (2015).
22. C.-M. J. Hu, R. H. Fang, K.-C. Wang, B. T. Luk, S. Thamphiwatana, D. Dehaini, P. Nguyen, P. Angsantikul, C. H. Wen, A. V. Kroll, C. Carpenter, M. Ramesh, V. Qu, S. H. Patel, J. Zhu, W. Shi, F. M. Hofman, T. C. Chen, W. Gao, K. Zhang, S. Chien, L. Zhang, Nanoparticle biointerfacing by platelet membrane cloaking. *Nature* **526**, 118–121 (2015).
23. Z. Wu, T. Li, W. Gao, T. Xu, B. Jurado-Sánchez, J. Li, W. Gao, Q. He, L. Zhang, J. Wang, Cell-membrane-coated synthetic nanomotors for effective biodetoxification. *Adv. Funct. Mater.* **25**, 3881–3887 (2015).
24. Z. Wu, J. Li, B. Esteban-Fernández de Ávila, T. Li, W. Gao, Q. He, L. Zhang, J. Wang, Water-powered cell-mimicking Janus micromotor. *Adv. Funct. Mater.* **25**, 7497–7501 (2015).
25. J. Li, P. Angsantikul, W. Liu, B. Esteban-Fernández de Ávila, X. Chang, E. Sandraz, Y. Liang, S. Zhu, Y. Zhang, C. Chen, W. Gao, L. Zhang, J. Wang, Biomimetic platelet-camouflaged nanorobots for binding and isolation of biological threats. *Adv. Mater.* **30**, 1704800 (2018).
26. V. Garcia-Gradilla, J. Orozco, S. Sattayasamitsathit, F. Soto, F. Kuralay, A. Pourazary, A. Katzenberg, W. Gao, Y. Shen, J. Wang, Functionalized ultrasound-propelled magnetically guided nanomotors: Toward practical biomedical applications. *ACS Nano* **7**, 9232–9240 (2013).
27. D. Dehaini, X. Wei, R. H. Fang, S. Masson, P. Angsantikul, B. T. Luk, Y. Zhang, M. Ying, Y. Jiang, A. V. Kroll, W. Gao, L. Zhang, Erythrocyte–platelet hybrid membrane coating for enhanced nanoparticle functionalization. *Adv. Mater.* **29**, 1606209 (2017).
28. K. J. Rao, F. Li, L. Meng, H. Zheng, F. Cai, W. Wang, A force to be reckoned with: A review of synthetic microswimmers powered by ultrasound. *Small* **11**, 2836–2846 (2015).
29. F. Nadal, E. Lauga, Asymmetric steady streaming as a mechanism for acoustic propulsion of rigid bodies. *Phys. Fluids* **26**, 082001–082028 (2014).
30. F. Soto, G. L. Wagner, V. Garcia-Gradilla, K. T. Gillespie, D. R. Lakshmipathy, E. Karshalev, C. Angell, Y. Chen, J. Wang, Acoustically propelled nanoshells. *Nanoscale* **8**, 17788–17793 (2016).
31. S. Ahmed, W. Wang, L. Bai, D. T. Gentekos, M. Hoyos, T. E. Mallouk, Density and shape effects in the acoustic propulsion of bimetallic nanorod motors. *ACS Nano* **10**, 4763–4769 (2016).
32. L. Ricotti, B. Trimmer, A. W. Feinberg, R. Raman, K. K. Parker, R. Bashir, M. Sitti, S. Martel, P. Dario, A. Menciassi, Biohybrid actuators for robotics: A review of devices actuated by living cells. *Sci. Robot.* **2**, eaaq0495 (2017).
33. D. Ahmed, T. Baasch, B. Jang, S. Pane, J. Dual, B. J. Nelson, Artificial swimmers propelled by acoustically activated flagella. *Nano Lett.* **16**, 4968–4974 (2016).
34. T. Qiu, S. Palagi, A. G. Mark, K. Melde, F. Adams, P. Fischer, Wireless actuation with functional acoustic surfaces. *Appl. Phys. Lett.* **109**, 191602 (2016).
35. J. J. Kwan, R. Myers, C. M. Coviello, S. M. Graham, A. R. Shah, E. Stride, R. C. Carlisle, C. C. Coussios, Ultrasound-propelled nanocups for drug delivery. *Small* **11**, 5305–5314 (2015).
36. I. R. Siboo, H. F. Chambers, P. M. Sullam, Role of SraP, a Serine-rich surface protein of *Staphylococcus aureus*, in binding to human platelets. *Infect. Immun.* **73**, 2273–2280 (2005).
37. J. R. Fitzgerald, T. J. Foster, D. Cox, The interaction of bacterial pathogens with platelets. *Nat. Rev. Microbiol.* **4**, 445–457 (2006).
38. C. Meesters, A. Brack, N. Hellmann, H. Decker, Structural characterization of the α-hemolysin monomer from *Staphylococcus aureus*. *Proteins* **75**, 118–126 (2009).
39. L. Song, M. R. Hobaugh, C. Shustak, S. Cheley, H. Bayley, J. E. Gouaux, Structure of staphylococcal α-hemolysin, a heptameric transmembrane pore. *Science* **274**, 1859–1866 (1996).
40. D. Pornpattananangkul, L. Zhang, S. Olson, S. Aryal, M. Obonyo, K. Vecchio, C.-M. Huang, L. Zhang, Bacterial toxin-triggered drug release from gold nanoparticle-stabilized liposomes for the treatment of bacterial infection. *J. Am. Chem. Soc.* **133**, 4132–4139 (2011).
41. P. O'Hanley, G. Lalonde, G. Ji, Alpha-hemolysin contributes to the pathogenicity of piliated digalactoside-binding *Escherichia coli* in the kidney: Efficacy of an alpha-hemolysin vaccine in preventing renal injury in the BALB/c mouse model of pyelonephritis. *Infect. Immun.* **59**, 1153–1161 (1991).
42. X. Wei, J. Gao, F. Wang, M. Ying, P. Angsantikul, A. V. Kroll, J. Zhou, W. Gao, W. Lu, R. H. Fang, L. Zhang, In situ capture of bacterial toxins for antivirulence vaccination. *Adv. Mater.* **29**, 1701644 (2017).
43. C.-M. J. Hu, L. Zhang, S. Aryal, C. Cheung, R. H. Fang, L. Zhang, Erythrocyte membrane-camouflaged polymeric nanoparticles as a biomimetic delivery platform. *Proc. Natl. Acad. Sci. U.S.A.* **108**, 10980–10985 (2011).
44. W. Gilpin, V. N. Prakash, M. Prakash, Flowtrace: Simple visualization of coherent structures in biological fluid flows. *J. Exp. Biol.* **220**, 3411–3418 (2017).

Funding: This work was supported by the Defense Threat Reduction Agency Joint Science and Technology Office for Chemical and Biological Defense (grant nos. HDTRA1-13-1-0002 and HDTRA1-14-1-0064). F.S. acknowledges fellowship from The University of California Institute for Mexico and the United States (UC MEXUS) and El Consejo Nacional de Ciencia y Tecnología (CONACYT). **Author contributions:** All authors contributed to the writing of the manuscript. All authors have given approval to the final version of the manuscript. **Competing interests:** The authors declare that they have no competing financial interests. **Data and materials availability:** All data needed to evaluate the study are in the paper or in the Supplementary Materials.

Submitted 18 January 2018
Accepted 27 March 2018
Published 30 May 2018
10.1126/scirobotics.aat0485

Citation: B. Esteban-Fernández de Ávila, P. Angsantikul, D. E. Ramírez-Herrera, F. Soto, H. Teymourian, D. Dehaini, Y. Chen, L. Zhang, J. Wang, Hybrid biomembrane–functionalized nanorobots for concurrent removal of pathogenic bacteria and toxins. *Sci. Robot.* **3**, eaat0485 (2018).

Science Robotics

Hybrid biomembrane–functionalized nanorobots for concurrent removal of pathogenic bacteria and toxins

Berta Esteban-Fernández de Ávila, Pavimol Angsantikul, Doris E. Ramírez-Herrera, Fernando Soto, Hazhir Teymourian, Diana Dehaini, Yijie Chen, Liangfang Zhang, and Joseph Wang

Sci. Robot. **3** (18), eaat0485. DOI: 10.1126/scirobotics.aat0485

Science Robotics (ISSN 2470-9476) is published by the American Association for the Advancement of Science. 1200 New York Avenue NW, Washington, DC 20005. The title *Science Robotics* is a registered trademark of AAAS.